Cambridge International
Science Publishing
Cambridge CB1 6AZ
Great Britain

Journal of Computational Methods in Sciences and Engineering
vol. 1, no. 2s-3s, 2001, pp. 267–286
ISSN 1472–7978

Analytic reconstruction algorithms in emission tomography with variable attenuation

Leonid A Kunyansky

Department of Mathematics
University of Arizona
Tucson, AZ 85721, USA.
E-mail: leonk@math.arizona.edu
Tel: (520) 621-4509

Received 27 March, 2001; accepted in revised form 8 October, 2001

Abstract: We present two analytic reconstruction algorithms applicable in emission tomography with variable attenuation. One of this algorithms is based on the recently discovered explicit inversion formula for the attenuated Radon transform with non-uniform attenuation; it is intended for applications in single-photon emission computed tomography. The second of the methods we present is applicable for approximate inversion of the generalized Radon transform with more general weights for which inversion formulae are not known; inversion of such transforms are required, for instance, in the emission tomography of gases. The latter algorithm is based on an approximate (up to a smoothing term) inversion of the underlying integral operator; in spite of its approximate nature it yields quite accurate reconstructions and exhibits very low sensitivity to noise in data. In fact, when applied to data containing significant level of noise the latter algorithm yields better reconstructions than the first of our mehods (based on theoretically exact inversion formula). We support conclusions of the paper by a number of convincing numerical results.

Keywords: Pseudo-differential operator, Radon transform, SPECT, Novikov inversion formula, analytic algorithm.

Mathematics Subject Classification: 45Q05, 65R32, 44A12, 65M32.

Introduction

Several types of tomography lead to a problem of image reconstruction from attenuated projections. One of the most important applications of this type is single-photon emission computed tomography (SPECT); another instance of such technique is optical (infra-red) tomography of hot gases or plasma. In both cases the measured intensity of radiation is described by weighted line integrals of the emission coefficient (activity distribution); the latter function is the quantity one seek to recover. The above-mentioned direction- and position- dependent integration weights arise due to the attenuation of radiation on its way from the source to the detector. Due to the presence of these weights in the resulting integral transformation (usually referred to as the attenuated Radon transform) the well known algorithms of classical X-ray tomography can no longer be used for the image reconstruction; specialized reconstruction techniques have to be utilized instead.

Most of known inversion algorithms for the attenuated Radon transform can be viewed as iterative procedures of various kinds. Iterative methods are flexible and frequently allow one to

treat more realistic mathematical models of the problem. The drawback of iterative techniques is relatively long reconstruction times; besides, rate (and, in general, existence) of convergence of such iterations depends significantly on the parameters of the problem. Analytic (non-iterative) approaches, on the other hand, are based on evaluation of explicit (exact or approximate) inversion formulae. Such methods are significantly faster and can perform extremely well in certain cases (as does, for instance, the filtered backprojection algorithm (FBP) in the case of X-ray tomography). However, the underlying inversion formulae are difficult (sometimes impossible) to derive for the realistic mathematical models of measurements.

In this paper we present two new analytic reconstruction algorithms for emission tomography. The first of these methods is based on the recently discovered explicit inversion formula [7] for the attenuated Radon transform and it is applicable for SPECT reconstruction. The second algorithm we introduce can be used for approximate inversion of a more general weighted Radon transforms; it amounts to evaluation of an approximate (up to a smoothing term) solution to the underlying integral equation. Although the underlying formula does not represent an exact solution, the latter approach yields surprisingly accurate approximations. Moreover, this technique exhibits very low sensitivity to noise present in the data which makes the algorithm suitable for practical applications associated with noisy data — including, importantly, SPECT. We demonstrate performance of the two proposed algorithms in a variety of numerical reconstructions of images from both exact and noisy data; our presentation is concluded with the results obtained by processing data of real SPECT measurements.

1 Mathematical models

SPECT is based on measurements of gamma-rays radiated by a radionuclide injected into a patient [1]; the sought after quantity is the spatially varying activity of the radionuclide in the patient's body. The geometry of measurements is shown in Figure 1; the measured data $P(p,\varphi)$ (referred to as the projections) can, roughly, be modeled by weighted line integrals of the activity $f(\mathbf{x})$ along the lines parametrized by a pair of parameters (p,φ) (such a model neglects effects of photon scattering and detector imperfections):

$$\begin{aligned} P(p,\varphi) &= R_w f(p,\varphi) \equiv \int\limits_{\mathbb{R}^2} f(\mathbf{x}) w(\mathbf{x},\omega(\varphi)) \delta\left(\mathbf{x}\cdot\omega^{\perp}(\varphi) - p\right) \mathrm{d}\mathbf{x}, \\ \omega^{\perp}(\varphi) &= (\cos\varphi, \sin\varphi), \end{aligned} \tag{1}$$

where weight $w(\mathbf{x},\omega(\varphi))$ accounts for the attenuation of radiation on its way from the source point $\mathbf{x}$ in the direction $\omega(\varphi) = (\sin\varphi, -\cos\varphi)$ toward the detector. In other words, projections $P(p,\varphi)$ are related to activity $f(\mathbf{x})$ by the integral transform $R_w f(p,\varphi)$ defined by (1); we will refer to this generalization of the Radon transform as to the weighted Radon transform with the weight $w(\mathbf{x},\omega(\varphi))$. In the case of SPECT this weight can be expressed in terms of the natural exponent of an integral of the attenuation coefficient $\mu(\mathbf{x})$ along the radiation path:

$$w(\mathbf{x},\omega(\varphi)) = \exp\left(-\int_0^{\infty} \mu\left[\mathbf{x} + s'\omega(\varphi)\right] \mathrm{d}s'\right). \tag{2}$$

Transformation (1) with the exponential weight defined by the particular expression (2) is referred to as the attenuated Radon transform; reconstructing activity distribution from projections $P(p,\varphi)$ is equivalent to inverting this transform. We assume throughout the paper that attenuation $\mu(\mathbf{x})$ (and, therefore weight $w(\mathbf{x},\omega(\varphi))$) is known.(in practice, $\mu(\mathbf{x})$ can, for example, be reconstructed from transmission measurements using methods of conventional X-ray tomography). In many important applications of various kinds of emission tomography, in particular in SPECT of the

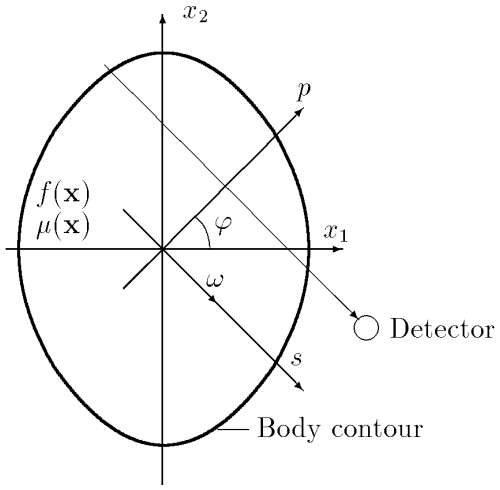

Figure 1: Geometry of measurements

human thorax, attenuation coefficient $\mu(\mathbf{x})$ varies significantly across the integration region; these variations cannot be neglected and have to be accounted for by a reconstruction algorithm.

Similarly to SPECT, infra-red tomography of gases and plasma also relies on measurements that can be modeled by the weighted line integrals (see, for instance [2],[3],[4]). The value of interest in this case is the emission coefficient which we also denote by $f(\mathbf{x})$. Due to a different nature of radiation and detectors, however, a value measured along a line represents an integral of the radiation intensity over certain range of frequencies; across this range values of both emission and attenuation coefficient oscillate wildly. In this case an approximate equation of the form (1) still can be derived (see, for instance [6] and references therein), but the expression (2) is no longer valid and has to be replaced by the following more general expression:

$$w(\mathbf{x}, \omega(\varphi)) = W\left(\int_0^\infty \mu\left[\mathbf{x} + s'\omega(\varphi)\right] \mathrm{d}s'\right), \tag{3}$$

where $W()$ is a certain decreasing positive function. We will refer to the transformation (1) with the weight given by expression (3) as the attenuated Radon transform with a non-exponential weight.

In all cases of emission tomography we mentioned the reconstruction of activity (emission) distribution from projections is equivalent to the inversion of the weighted Radon transform with the corresponding weight. In the following section we discuss the particular case of the attenuated Radon transform with exponential weight (2). The case of more general weights is investigated in Section 3.

2 Attenuated Radon transform with exponential weight

Due to the practical importance of SPECT the case of the exponential weight (2) enjoyed most of attention of researchers. The first analytic methods for the attenuation correction in the case of a constant attenuation coefficient $\mu(\mathbf{x}) = \mu_0$ were proposed by Bellini *et al* [11] and Tretiak and Metz [12]; both algorithms assumed that the attenuation coefficient was constant inside a patient's body and that the cross-section of the body was convex. Later on, a series of more advanced analytic reconstruction techniques for the constant attenuation case have been introduced ([13],

[14], [15], [16], [17],[18]); certain extensions to the underlying assumptions of constant attenuation and convex body were treated in [18] and [19]. With few exceptions (such as crude approximating techniques of [20],[23] and [24]) there were practically no analytic approaches available for the important case of (significantly) varying attenuation coefficient until recently. The breakthrough in the inversion of the attenuated Radon transform with the exponential weight was made in [9], [7] were exact inversion formulae were derived. (see also [10]). In particular, a relatively straightforward discretization of the Novikov's inversion formula [7] results in an algorithm ([8], [10]) capable of non-iterative image reconstruction even within the regions with strongly non-uniform attenuation distributions, similar to the one found within a human thorax. Thus, in Sections 2.1 and 2.2 we provide a brief discussion of the Novikov explicit inversion formula [7] and a short description of the inversion algorithm [8], respectively. In Section 2.3 we introduce certain extensions to the above-mentioned basic reconstruction algorithm intended to improve the noise propagation properties of the method.

2.1 Novikov explicit inversion formula

In order to simplify presentation we introduce a rotated coordinate system (s,p) with axes parallel to vectors $\theta(\varphi)$ and $\theta^{\perp}(\varphi)$ (see Figure 1) so that

$$\begin{aligned} s &= x\cos\varphi + y\sin\varphi, \\ p &= -x\sin\varphi + y\cos\varphi. \end{aligned}$$

In the new coordinates the integrations defined by equations (1, 2) can be written in a particularly simple form:

$$P(p,\varphi) \equiv \int_{\mathbb{R}} \exp\left(-D^*_\varphi \mu^*_\varphi(s,p)\right) f^*_\varphi(s,p)\mathrm{d}s, \tag{4}$$

$$D^*_\varphi \mu^*_\varphi(s,p) = \int_s^\infty \mu^*_\varphi(s',p)\mathrm{d}s', \tag{5}$$

where $f^*_\varphi(s,p) = f(\mathbf{x}(s,p,\varphi))$, $\mu^*_\varphi(s,p) = \mu(\mathbf{x}(s,p,\varphi))$, and $D^*_\varphi \mu^*_\varphi(s,p) = D_\varphi \mu(\mathbf{x}(s,p,\varphi))$.

The (classical) Radon transform $Rv(p,\varphi)$ of a function $v(\mathbf{x})$ is defined by the following equation

$$Rv(p,\varphi) = \int_{-\infty}^{\infty} v(\mathbf{x}(s',p,\varphi))\mathrm{d}s'.$$

Comparing this expression to (5) one observes that the values of $R\mu(p,\varphi)$ coincide with limiting values of the divergent beam transform D_φ :

$$R\mu(p,\varphi) = D^*_\varphi \mu^*_\varphi(-\infty,p).$$

Using the above notation, the Novikov inversion technique is given by the following set of formulae:

$$f(\mathbf{x}) = \frac{1}{4\pi}\int_0^{2\pi} M_\varphi(\mathbf{x}\cdot\theta(\varphi), \mathbf{x}\cdot\theta^{\perp}(\varphi))\mathrm{d}\varphi, \tag{6}$$

$$M_\varphi(s,p) = \frac{\partial}{\partial p}\left[\exp(D^*_\varphi \mu^*_\varphi(s,p)) m_\varphi(p)\right], \tag{7}$$

$$\begin{aligned} m_\varphi(p) = {} & \mathrm{e}^{-A_\varphi(p)}\left[h^c_\varphi(p) H\left(h^c_\varphi(p)\mathrm{e}^{A_\varphi(p)} P(p,\varphi)\right),\right. \\ & \left. + \; h^s_\varphi(p) H\left(h^s_\varphi(p)\mathrm{e}^{A_\varphi(p)} P(p,\varphi)\right)\right] \end{aligned} \tag{8}$$

with

$$\begin{aligned} h^c_\varphi(p) &= \cos(HA_\varphi(p)),\ h^s_\varphi(p) = \sin(HA_\varphi(p)), \\ A_\varphi(p) &= \frac{1}{2}R\mu(p,\varphi). \end{aligned}$$

In the above formulae H denotes the Hilbert transform, defined for a given function $\psi(u)$ as follows:

$$H\psi(u) = \mathcal{P}\int_{\mathbb{R}} \psi(v)/(\pi(u-v))\mathrm{d}v. \tag{9}$$

2.2 Basic reconstruction algorithm

According to equations (6)-(9) one can reconstruct radionuclide distribution $f(\mathbf{x})$ from the projections $P(p,\varphi)$ by:

1. Evaluating the divergent beam transform $D^*_\varphi\mu^*_\varphi(s,p)$ and the Radon transform $R\mu(p,\varphi)$;
2. Evaluating the Hilbert transform of $A_\varphi(p)$;
3. Computing functions $m_\varphi(p)$ (see equation (8));
4. Differentiating the product $\exp(D^*_\varphi\mu^*_\varphi(s,p))m_\varphi(p)$ in p, (see (7));
5. Backprojecting the result of the differentiation $M_\varphi(s,p)$ (see equation 6).

Our basic reconstruction algorithm (see [8] for details) follows the structure of the inversion formula; we use finite differences to compute derivatives in step 4, and trapezoidal rules together with bilinear interpolations to evaluate integrals in steps 1 and 5. (see also [10]). The Hilbert transforms in steps 2 and 3 are approximated by a discrete convolution with a regularized and discretized version of the exact kernel $1/(\pi p)$; this discrete kernel is represented by the following sequence of values K_j:

$$\begin{aligned} K_j &= \frac{1}{\pi}\left[j\ln(1-\frac{1}{j^2}) + \ln\frac{j+1}{j-1}\right],\ j = 2,...,n_p \\ K_1 &= \frac{2}{\pi}\ln 2,\ K_0 = 0,\ K_{-j} = -K_j,\ j = -n_p,...1. \end{aligned}$$

2.3 Improving stability of the algorithm

The basic version of our algorithm presented above allows for accurate non-iterative image reconstruction in the case of strongly nonuniform attenuation distributions, similar to the attenuation within a human thorax. However, as our numerical tests show (see Section 2.4), the algorithm is quite sensitive to noise contained in the data. In particular, level of noise in the image obtained from this method are significantly higher than that in the image reconstructed using the FBP from non-attenuated projections (containing the same level of noise).

In this section we propose a numerical technique allowing one to improve the noise propagation properties of the reconstruction. In order to achieve this goal we first (using the basic version of the algorithm) reduce the reconstruction problem to the inversion of a classical (non-attenuated) Radon transform. The latter inversion problem is significantly less ill-posed and can be solved numerically using, for example, the FBP algorithm, which yields significantly less noisy reconstruction.

In order to obtain the desired reduction to classical Radon transform we apply the multiplicative correction method described below. (This method is closely related to the technique used in [21] as a part of an iterative reconstruction algorithm).

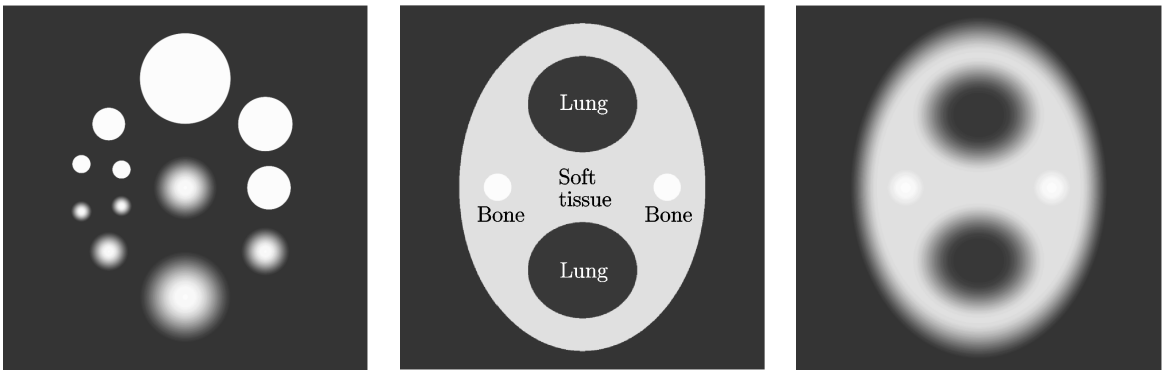

Figure 2: Model distributions (a) activity phantom (b) attenuation phantom from [22] (c) smooth attenuation fantom.

For activity distribution $f(\mathbf{x})$ the unattenuated projections $Rf(p,\varphi)$ are defined by the formula (1) with $w(\cdot) = 1$. Let us introduce a correction coefficient $k(p,\varphi)$ defined by the following equation

$$k(p,\varphi) = (Rf(p,\varphi) + c) \,/\, (R_w f(p,\varphi) + c)\,, \tag{10}$$

$c > 0$, so that $R(p,\varphi) = k(p,\varphi)\,[R_w f(p,\varphi) + c] - c$. Obviously, since $f(\mathbf{x})$ is nonnegative, the following inequality holds

$$1 \le k(p,\varphi) \le \exp(R\mu(p,\varphi)). \tag{11}$$

Values of $k(p,\varphi)$ are unknown, of course; however, given a good approximation to $f(\mathbf{x})$ one can easily compute an approximation to $k(p,\varphi)$. Thus, our strategy when dealing with noisy data is described as follows:

(A) Compute an approximate version $f^{appr}(\mathbf{x})$ of the image using the basic version of the present algorithm; enforce the condition $f^{appr}(\mathbf{x}) \ge 0$;

(B) Compute $Rf^{appr}(p,\varphi)$ and $R_w f^{appr}(p,\varphi)$ from equation (1);

(C) Compute $k^{appr}(p,\varphi)$ from equation (10) enforcing conditions (11);

(D) Find approximate values of unattenuated projections $Rf(p)$ by multiplying $P(p,\varphi)$ by $k^{appr}(p,\varphi)$;

(E) Reconstruct the new image from unattenuated projections using the classical FBP algorithm.

As integral quantities, computed projections $Rf^{appr}(p,\varphi)$ and $R_w f^{appr}(p,\varphi)$ are much less affected by noise in the data than the point values of $f^{appr}(\mathbf{x})$, which leads to an accurate reconstruction of the correction factor $k^{appr}(p,\varphi)$. Therefore, the noise levels in the product $P(p,\varphi)k^{appr}(p,\varphi)$ and in the projections $P(p,\varphi)$ are of the same level. On the other hand, the FBP algorithm utilized for the image reconstruction from unattenuated projections $P(p,\varphi)k^{appr}(p,\varphi)$ is much less sensitive to noise in the data; thus, it yields image of much better quality than the initial approximation $f^{appr}(\mathbf{x})$.

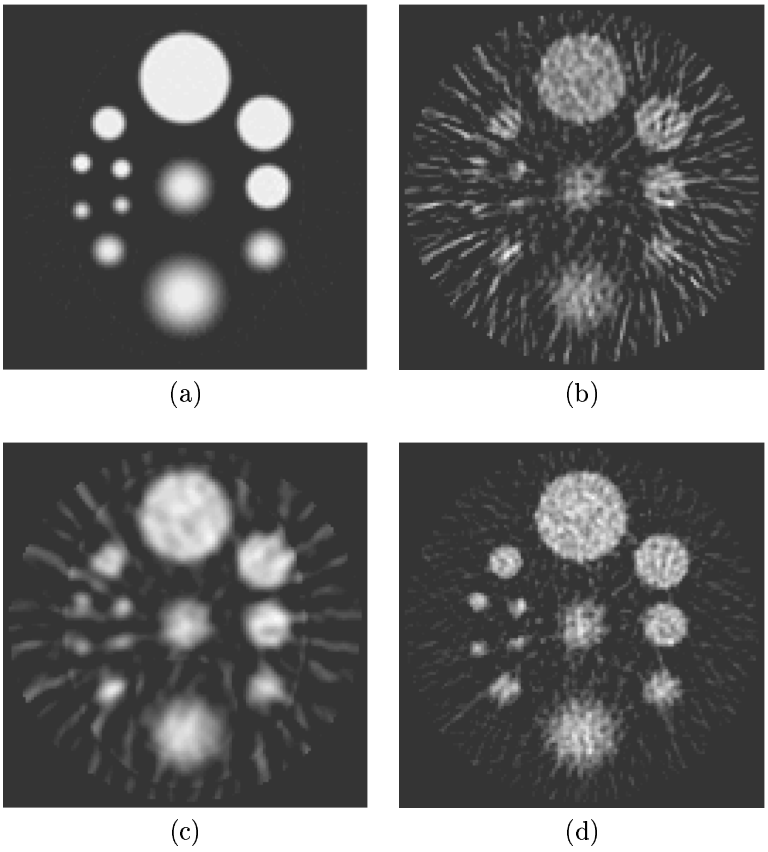

Figure 3: Images reconstructed using Novikov's formula in the case of discontinious attenuation (a) from exact data (b) from noisy data (c) from noisy data, low-pass filter applied (d) from noisy data, utilizing multiplicative correction technique of Section 2.3

2.4 Numerical examples

In order to test the algorithm the following model distributions will be utilized. The activity phantom (Figure 2(a)) consists of a set of test objects. Some of these objects are defined by characteristic functions of circles, while the others are given by bell-shaped C^∞ functions

$$u_i(\mathbf{x}, \mathbf{x}_i, r_i) = \exp\left(\frac{2\exp\left(-\frac{1}{t}\right)}{t-1}\right), \quad t = |\mathbf{x} - \mathbf{x}_i| / r_i,$$

for $|\mathbf{x} - \mathbf{x}_i| \leq r_i$. This phantom which contains both smooth and discontinuous functions with various size of support will enable us to probe the ability of the algorithm to reproduce both smaller details (fast varying discontinuous distributions) and larger details (areas of slowly or constant activity).

To simulate a realistic strongly non-uniform attenuation coefficient we utilize the phantom used in [22]. This model imitates the attenuation distribution across a section of a human thorax; it consists of an ellipsoidal body with axes of length 22.5 cm and 30 cm. The smaller ellipsoidal regions (see Figure 2(b)) simulate lungs, while the circular regions correspond to bones; attenuation is equal to 0.01 cm^{-1} within "lungs" and to 0.17 cm^{-1} within "bones". Attenuation within the

rest of the large ellipse is equal to 0.15 cm^{-1}.

In order to check performance of our methods in the case of a smoothly varying attenuation coefficient we will use a function shown in Figure 2(c); this phantom represented by a C^∞ infinity function resembles the discontinuous phantom shown in Figure 2(b) and has similar values of attenuation in the flat regions of the image.

Quantum noise in the projection data in our experiments was simulated in the following way (i) the projections were scaled (multiplied by a constant factor) so that the maximum "measured" value in the data set was equal to 20 (ii) each point value in the data set was then replaced by a random realization of a Poisson variate with a mean equal to that value.

A variety of numerical tests we performed demonstrated that the basic version of our algorithm (see Section 2.2) yields accurate non-iterative image reconstruction from exact projections in the case of realistic strongly nonuniform attenuation distribution. An example of such reconstruction is presented in Figure 3(a); it was obtained from the set of 400 projections (129 samples each) generated from model distributions shown in Figure 2(a), 2(b). The quality of the reconstruction is very high; there is no trace in the image of the underlying discontinuous attenuation. (More numerical examples of this kind can be found in [8], [10].)

Figure 3(b) presents results obtained using the basic version of our algorithm from the same data as the ones used in the previous test; the only difference was that now Poisson noise was added to the projections (the relative L^2 intensity of the noise produced as described above was equal to 33.6%). One can see that in this case the reconstructed image contains significant amount of noise; the image is much noisier, for instance, than the images presented in Figures 3(d), 4(c). The reconstructions obtained using the FBP from non-attenuated projections containing a comparable level of noise (not presented here) are also considerably less noisier.

One of the conventional ways of reducing noise sensitivity of an algorithm is a low-pass filtration of the data. In our case such filtration does not produce satisfactory results, see Figure 3(c). The latter image was obtained by applying to projections a low-frequency filter $\eta(\cdot)$ defined by its Fourier transform $\hat{\eta}(\rho)$ as follows:

$$\hat{\eta}(\rho) = \begin{cases} \frac{1}{2}\left(1+\cos(\pi\rho/\rho^{cutoff})\right) & , \quad |\rho| \le \rho^{cutoff} \\ 0 & , \quad |\rho| > \rho^{cutoff} \end{cases} , \tag{12}$$

where ρ^{cutoff} is the cut-off frequency, $\rho^{cutoff} \le \rho^{Nyquist}$; the cut-off frequency ρ^{cutoff} was equal to a half of the Nyquist frequency $\rho^{Nyquist}$ in the example we present. As one observes, the low-frequency filtration leads to a certain loss of a finer detail in the image but does not reduce sufficiently the noise level. In contrast, the multiplicative correction technique of Section 2.3 does considerably reduce noise in the image without loss of detail, see Figure 3(d). Similar effects result from application of the techniques we discuss to the data of real measurements, see Section 4.

3 General weights: inverse amplitude algorithm

Much less is known about the Radon transform with general weights than about the attenuated Radon transform (with exponential weights of the form 2). The invertibility of the former transform was proven for the case of rotation invariant weights [29] and for the case of positive real analytic weights [27]. A local invertibility of this transform was also established [26]. On the other hand, it was shown in [28] that positive C^∞ weight does not guarantee the invertibility of the transform. Naturally, one can prove invertibility of the weighted transform if the weights are in some sense closed to one (see [32] for the details). Numerical issues associated with the inversion of the weighted Radon transform are studied even less. Although most of iterative algorithms (not considered here) can be generalized for the inversion of the latter transform, no exact inversion formulae is known in this case.

In this section we introduce an algorithm applicable for approximate inversion of the weighted Radon transform. There is a two-fold practical goal of the development of this technique. First, this method can be used in applications that leads to non-exponential weights, such as infra-red tomography of gases, flames and plasma. On the other hand, this technique can also be used for SPECT reconstruction. In spite of its approximate nature the method yields quite accurate reconstructions and exhibits very low sensitivity to noise in data. In fact, as shown by numerical experiments presented in this paper, when applied to data containing significant level of noise the algorithm we introduce yields better reconstructions than the methods based on theoretically exact inversion formula (described in Section 2).

Let us consider the classical FBP algorithm that maps projections $P(p,\varphi)$ into image $g(\mathbf{x})$ according to the following two formulae:

$$g(\mathbf{y}) = \frac{1}{2}\int_0^{2\pi} m(\mathbf{y}\cdot\omega^{\perp}(\varphi),\varphi)\mathrm{d}\varphi, \tag{13}$$

$$m(p,\varphi) = \int_{\mathbb{R}} |\rho|\, \mathrm{e}^{2\pi \mathrm{i} p\rho}\widehat{P}(\rho,\varphi)\mathrm{d}\rho, \tag{14}$$

where $\widehat{P}(\rho,\varphi)$ is the 1-D Fourier transform of projections:

$$\widehat{P}(\rho,\varphi) = \int_{\mathbb{R}} \mathrm{e}^{-2\pi \mathrm{i} p\rho}P(p,\varphi)\mathrm{d}p. \tag{15}$$

We will denote the corresponding operator by R^{-1}_{FBP} so that

$$g(\mathbf{y}) = (R^{-1}_{FBP}P(p,\varphi))(\mathbf{y}).$$

Operator R^{-1}_{FBP} is a left inverse operator to the classical Radon transform; in other words if attenuation is absent, i.e.$w(\cdot) = 1$, then $\left(R^{-1}_{FBP}P(p,\varphi)\right)(\mathbf{y}) = R^{-1}_{FBP}Rf = f$. One can try to also use the FBP algorithm to obtain an approximate reconstruction in the case when attenuation is present. Naturally, the result $g(\mathbf{y}) = R^{-1}_{FBP}R_w f$. will not be quantitatively accurate. It is known, however, that the singularities present in the original image f will be preserved in the approximation g. The explanation of this phenomenon is also well known. Indeed, it is readily verifiable (see Appendix) that

$$\begin{aligned} g(\mathbf{y}) &= \left(R^{-1}_{FBP}R_w f\right)(\mathbf{y}) \\ &= \int_{\mathbb{R}^2}\int_{\mathbb{R}^2} \mathrm{e}^{2\pi \mathrm{i}(\mathbf{y}-\mathbf{x})\cdot\xi} f(\mathbf{x}) W\left(\mathbf{x}, \frac{\xi^{\perp}}{|\xi|}\right)\mathrm{d}\xi\mathrm{d}\mathbf{x} \end{aligned} \tag{16}$$

where

$$\begin{aligned} \xi(\rho,\varphi) &= \rho\omega^{\perp}(\varphi) = (\rho\cos\varphi, \rho\sin\varphi), \\ W(\mathbf{x},\omega) &\equiv \frac{1}{2}\left[w(\mathbf{x},\omega) + w(\mathbf{x},-\omega)\right]. \end{aligned}$$

In the case of C^{∞} infinity weight $w(\cdot)$ representation (16) allows us to identify.$R^{-1}R_w$ as a pseudo-differential operator (ΨDO) of order 0 with an amplitude $W(\mathbf{x}, \xi/|\xi|)$ (see, for instance [30] for introduction into theory of ΨDO's). Such operators are known to preserve singularities of a function. Another useful fact from the theory of ΨDO is that such operators (of order 0) are continuous from L^2 into L^2.

From the practical point of view the advantage of computing $R^{-1}R_w f$ is that due to low noise sensitivity of the FBP the image $g(\mathbf{y}) = R^{-1}_{FBP}R_w f$ is less noisy than, for example, reconstructions obtained using existing exact inversion formula. One faces then a problem of reconstructing f from g; if such reconstruction is possible (which is not necessarily true for general C^∞ weights since, as shown in [28] the weighted Radon transform is not always invertible), it represents a well posed problem (unlike the ill-posed original reconstruction problem).

Our method of computing an approximation to f from g is related to the idea of a parametrix of an operator, one of the basic tools developed in the theory of ΨDO. In detail, although it is not known how to obtain an explicit inverse for an arbitrary ΨDO, one can construct an approximate inverse in the form of series of ΨDO of decreasing orders which is called a parametrix (see [30]). The composition of a parametrix with the original operator is the identity operator plus an infinitely smoothing operator which maps distributions into C^∞ functions. In other words, the parametrix acts as an approximate inverse of a given operator; it reconstructs original image modulo some C^∞ function. Obviously, a parametrix of an operator is not uniquely defined. Moreover, general theory does not guarantee that the smooth residual of the parametrix will be small in any reasonable norm. However, as our numerical experiments show the particular approximate inversion we propose indeed results in surprisingly accurate reconstructions.

According to standard theory of ΨDO a parametrix B of a pseudo-differential operator A in the form

$$Ah(\mathbf{y}) = \int\limits_{\mathbb{R}^2}\int\limits_{\mathbb{R}^2} \mathrm{e}^{2\pi \mathrm{i}(\mathbf{y}-\mathbf{x})\cdot\xi} h(\mathbf{x}) a\left(\mathbf{x},\xi\right) \mathrm{d}\xi \mathrm{d}\mathbf{x},$$

can be defined as a series of operators B_j of increasing smoothness

$$B = \sum_{j=1}^{\infty} B_j, \tag{17}$$

where the operators B_j can be written in the following form

$$B_j h(\mathbf{y}) = \int\limits_{\mathbb{R}^2}\int\limits_{\mathbb{R}^2} \mathrm{e}^{2\pi \mathrm{i}(\mathbf{y}-\mathbf{x})\cdot\xi} h(\mathbf{x}) b_j\left(\mathbf{x},\xi\right) \mathrm{d}\xi \mathrm{d}\mathbf{x},$$

with certain functions (amplitudes) $b_j\left(\mathbf{x},\xi\right)$. In particular, the first amplitude $b_0\left(\mathbf{x},\xi\right)$ is equal simply to the inverse amplitude of the operator A:

$$b_0\left(\mathbf{x},\xi\right) = 1/a\left(\mathbf{x},\xi\right).$$

Obviously, in practical computations series (17) has to be truncated. In our algorithm we compute only the first term of a parametrix instead of the whole series. (As our numerical experiments presented in Sections 3.3 and 4.show, such a crude approximation turns out to be very accurate in the case of typical SPECT measurements. On the other hand, taking into account more terms of the parametrix did not result in essential improvements in the numerical tests). Thus, since the amplitude of the operator $R^{-1}_{FBP}R_w$ is equal to $W\left(\mathbf{x},\xi^\perp/|\xi|\right)$, the first term B_0 of the parametrix of this operator will have the amplitude $b_0\left(\mathbf{x},\xi\right) = 1/W\left(\mathbf{x},\xi^\perp/|\xi|\right)$, in other words

$$B_0 h(\mathbf{y}) = \int\limits_{\mathbb{R}^2}\int\limits_{\mathbb{R}^2} \mathrm{e}^{2\pi \mathrm{i}(\mathbf{y}-\mathbf{x})\cdot\xi} \frac{1}{W\left(\mathbf{x},\xi^\perp/|\xi|\right)} h(\mathbf{x}) \mathrm{d}\xi \mathrm{d}\mathbf{x}. \tag{18}$$

Comparing this equation with (16) one can easily see that operator B_0 can be represented as a composition $R^{-1}_{FBP}R_{1/W}$, where operator $R_{1/W}$ is defined by equation (1) with weight $w\left(\mathbf{x},\omega\right)$ replaced by $1/W(\mathbf{x},\omega)$.

According to the above discussion function $h(\mathbf{x}) = R_{FBP}^{-1} R_{1/W} g$ is related to $f(\mathbf{x})$ as:

$$h(\mathbf{x}) = (I + T) f(\mathbf{x}), \tag{19}$$

where I is the identity operator, and T is a compact operator mapping functions from a Sobolev space H^m to H^{m+1} and defined by the expression

$$T = I - R_{FBP}^{-1} R_{1/W} R_{FBP}^{-1} R_W.$$

Generally, one can try to solve Fredholm integral equation (19) with respect to $f(\mathbf{x})$ using some iterative solver. Our numerical experiments show, however, that function $h(\mathbf{x})$ is by itself a quite accurate approximation to the solution $f(\mathbf{x})$. Thus, our reconstruction technique involves processing projections $P(p, \varphi)$ with the FBP algorithm (13)-(15) (which yields a distorted image $g(\mathbf{x})$), followed by computation of an approximate solution $f^{approx}(\mathbf{x})$ to the equation (16) given by the result of application of $R_{FBP}^{-1} R_{1/W}$ to $g(\mathbf{x})$:

$$f^{approx} = R_{FBP}^{-1} R_{1/W} g. \tag{20}$$

We will refer to this method as the inverse amplitude algorithm.

It should be noticed that there are other ways of reducing the inversion problem to a Fredholm integral equation of the form (19) (with a different operator T). For example, in [31], [24] such a reduction is achieved by using weighted backprojection similar to the exponentially weighted backprojection used in the Novikov inversion formula, see equations (6), (7). However, while in the absence of noise such a weighted backprojection would yield good approximations (or an exact reconstruction in the case of Novikov formula), in the presence of intensive noise in the data the reconstructed image will be significantly distorted. In contrast, sequence of operators $R_{FBP}^{-1} R_{1/W} R_{FBP}^{-1} R_W$ does not contain weighted backprojection, which result in considerably lower noise sensitivity of the approximation computed using (19). The following section contains some analytic explanation for the advantage of methods based on unweighted backprojection. Numerical evidences supporting this claim are presented in Sections 3.3 and 4.

3.1 Noise sensitivity of the weighted backprojection

In order to develop an insight on the advantages of unweighted (rather than weighted) backprojection, let us compare the results of processing noisy attenuated projections of a point source by two algorithms: the FBP and the Tretiak-Metz scheme. For simplicity we will consider the case of constant attenuation $\mu(\mathbf{x}) = \mu_0$ (in this case the Tretiak-Metz scheme coincides with the Novikov formula). Assume that the activity distribution is given by a delta function located at the origin, i.e. $f(\mathbf{x}) = \delta(\mathbf{x} - \mathbf{x}_0)$. Then, the exact projections are equal to $(R_w f)(p, \varphi) = \delta(p - \mathbf{x}_0 \cdot \omega^{\perp}(\varphi)) \eta_1(\mathbf{x}_0, \varphi)$, where function $\eta_1(\mathbf{x}_0, \varphi)$ depends on the attenuation μ_0 and on the shape of the body contour. We will model the Poisson noise in the projections by multiplying them by a factor $\eta_2(\mathbf{x}_0, \varphi)$.

Consider first the result $u_{FBP}(\mathbf{x})$ of application of the FBP algorithm to the noisy projections $\delta(p)\eta_1(\mathbf{x}_0, \varphi)\eta_2(\mathbf{x}_0, \varphi)$. One can show [32] that

$$\begin{aligned} u_{FBP}(\mathbf{x}) &= R_{FBP}^{-1}[\delta(p - \mathbf{x}_0 \cdot \omega^{\perp}(\varphi)) \eta_1(\mathbf{x}_0, \varphi) \eta_2(\mathbf{x}_0 \varphi)] \\ &= R_{FBP}^{-1}[\eta_1(\mathbf{x}_0, \varphi) \eta_2(\mathbf{x}_0, \varphi) (R\delta(\mathbf{x} - \mathbf{x}_0))(p, \varphi)] \\ &= a_0(\mathbf{x}_0)\delta(\mathbf{x} - \mathbf{x}_0) + \sum_{k=-\infty}^{\infty} a_{2k}(\mathbf{x}_0) d_{2k,0}(\rho, \theta), \end{aligned}$$

where $a_{2k}(\mathbf{x}_0)$ are the even Fourier coefficients of the function $\eta_1(\mathbf{x}_0,\varphi)\eta_2(\mathbf{x}_0,\varphi)$ in the angular variable:

$$a_k(\mathbf{x}_0) = \frac{1}{2\pi}\int_0^{2\pi} \eta_1(\mathbf{x}_0,\varphi)\eta_2(\mathbf{x}_0,\varphi)|\mathrm{e}^{ik\theta}\mathrm{d}\varphi, \qquad k\in\mathbb{Z},$$

and functions $d_{k,0}(\rho,\theta)$ are defined in the polar coordinates ρ,θ as follows:

$$\begin{aligned} d_{k,0}(\rho,\theta) &= |k|\mathrm{e}^{ik\theta}\frac{1}{\rho^2}, \qquad k\in\mathbb{Z}, \\ \rho &= |\mathbf{x}-\mathbf{x}_0|, \qquad \mathbf{x}-\mathbf{x}_0 = (\rho\cos\theta,\rho\sin\theta). \end{aligned}$$

In other words, the point response $u_{FBP}(\mathbf{x})$ of the combination of measurements and the reconstruction algorithm (FBP in this case) decreases as a square of the distance from the point.

Consider now the result $u_{TM}(\mathbf{x})$ of the application of the Tretiak-Metz algorithm (we denote the corresponding operator by R_{TM}^{-1}) to the same noisy projections of $\delta(\mathbf{x}-\mathbf{x}_0)$.

$$\begin{aligned} u_{TM}(\mathbf{x}) &= R_{TM}^{-1}[\delta(p-\mathbf{x}_0\cdot\omega^{\perp}(\varphi))\eta_1(\mathbf{x}_0,\varphi)\eta_2(\mathbf{x}_0\varphi)] \\ &= R_{TM}^{-1}[\eta_2(\mathbf{x}_0,\varphi)(R_w\delta(\mathbf{x}-\mathbf{x}_0))(p,\varphi)] \\ &= b_0(\mathbf{x}_0)\delta(\mathbf{x}-\mathbf{x}_0) + \sum_{\substack{k=-\infty\\ k\neq 0}}^{\infty} b_k(\mathbf{x}_0)d_{k,\mu_0}(\rho,\theta). \end{aligned}$$

Functions $d_{k,\mu_0}(\rho,\theta)$ in the above equation admit the following representation [5]

$$d_{k,\mu_0}(\rho,\theta) = C_{k,l,m}(\mu_0)\mathrm{e}^{ik\theta}\sum_{l=0}^{\left[\frac{k}{2}\right]}\sum_{m=0}^{l}\rho^{|k|+2(m-l-1)}, \qquad k\in\mathbb{Z}\backslash 0,$$

with certain constants $C_{k,l,m}(\mu_0)$ depending on the attenuation coefficient μ_0, (see [5] for the details). The important property of functions $d_{k,\mu_0}(\rho,\theta)$ is that similarly to $d_{k,0}(\rho,\theta)$ they oscillate as $\mathrm{e}^{ik\theta}$ in θ but unlike $d_{k,0}(\rho,\theta)$ they grow as fast as $\rho^{|k|-2}$ in the radial direction. Such a point source response explains occurrence of star-like artifacts in the images reconstructed using the algorithm based on the Tretiak-Metz scheme or on Novikov explicit formula, see Sections 2.4. Similar behavior is expected from other methods employing weighted backprojection (such as [31], [24]). The inverse amplitude algorithm based on the unweighted backprojection, on the other hand, has point response decreasing fast in the radial direction, and accordingly, as demonstrated by numerical examples of Sections 3.3 and 4, this method exhibits low noise sensitivity. Such fast decrease of the point response also explains to some extent the high accuracy of approximations obtained from this method in case of strongly non-uniform attenuation. Indeed, locally the algorithm provides good reconstruction since the principal symbol of the operator $R_{FBP}^{-1}R_{1/W}R_{FBP}^{-1}R_W$. is equal to 1. On the other hand, each of the operators $R_{FBP}^{-1}R_W$ and $R_{FBP}^{-1}R_{1/W}$ can be represented as an integral operator with the kernels decreasing as ρ^{-2} in the radial direction so that non-local distortion also die out fast.

3.2 Computation of $R_{FBP}^{-1}R_{1/W}$ in spectral domain

Equations (13)-(15), and (20) define the basic version of the inverse amplitude algorithm; some results obtained using this technique are presented in Sections 3.3 and 4.There are, however, certain shortcomings in the straightforward computation of $R_{FBP}^{-1}R_{1/W}g$. Namely, evaluation of the inverse Radon transform R^{-1} is a known ill-posed problem; combined with the interpolations required when computing both the direct and inverse Radon transforms, it leads to a certain loss

of finer details. On the other hand, operator $R_{FBP}^{-1}R_{1/W}$ is a ΨDO of zero order; as we mentioned before, such operators are continuous from L_2 to L_2 which suggests that evaluation of $R_{FBP}^{-1}R_{1/W}g$ can be performed without resorting to ill-posed operations. Indeed, this can be done in a stable way utilizing techniques proposed in [32], [25] as described below.

Notice that $R_{FBP}^{-1}R_{1/W}g$ can be represented in the following form

$$\begin{aligned}\left(R_{FBP}^{-1}R_{1/W}g\right)(\mathbf{y}) &= \int\limits_{\mathbb{R}^2}\int\limits_{\mathbb{R}^2} \mathrm{e}^{2\pi\mathrm{i}(\mathbf{y}-\mathbf{x})\cdot\xi} g(\mathbf{x}) \frac{1}{W\left(\mathbf{x}, \xi^{\perp}/|\xi|\right)} \mathrm{d}\xi\mathrm{d}\mathbf{x} \\ &= F_2^{-1}\left(\int\limits_{\mathbb{R}^2} \mathrm{e}^{-2\pi\mathrm{i}\mathbf{x}\cdot\xi} g(\mathbf{x}) \frac{1}{W\left(\mathbf{x}, \xi^{\perp}/|\xi|\right)}\right)(\mathbf{y}) \qquad (21)\end{aligned}$$

Let us approximate function $V(\mathbf{x},\varphi) = 1/W(\mathbf{x}, [\xi/|\xi|](\varphi)) = 1/W(\mathbf{x}, \omega(\varphi+\pi/2))$ by its Fourier series in the angular variable as follows:

$$V(\mathbf{x},\varphi) \approx \sum_{k=-N}^{N} V_k(\mathbf{x})\mathrm{e}^{-\mathrm{i}2k\varphi}$$

(only even harmonics are present in the above equation since $W(\mathbf{x}, \omega(\varphi))$ is an even function in φ). Now $R_{FBP}^{-1}R_{1/W}g$ can be approximated by a sum of the Fourier transforms:

$$\begin{aligned} f^{approx}(\mathbf{x}) &= R_{FBP}^{-1}R_{1/W}g(\mathbf{y}) \\ &\approx F_2^{-1}\left(\sum_{k=-N}^{N} \mathrm{e}^{-\mathrm{i}2k\varphi(\xi)} \left(F_2[V_k(\mathbf{x})g(\mathbf{x})]\right)(\xi)\right)(\mathbf{y}) \\ &= V_0(\mathbf{y})g(\mathbf{y}) + 2\mathrm{Re}\left[F_2^{-1}\left(\sum_{k=1}^{N} \mathrm{e}^{-\mathrm{i}2k\varphi(\xi)} \left(F_2[V_k g]\right)(\xi)\right)(\mathbf{y})\right]. \qquad (22)\end{aligned}$$

Computations according to the above equation are stable and can be performed efficiently using the Fast Fourier transforms (FFT). The number of terms N in the series (22) can be chosen as small as 3 to 5 (see examples in the next section) in the case when $W(\mathbf{x}, \omega(\varphi))$ depends smoothly on φ. In the case when this function is not smooth the number of terms has to be increased to a value compared to the number of measured projections $N = \mathcal{O}(n)$. In the latter case the number of operations required for evaluations of $R_{FBP}^{-1}R_{1/W}g(\mathbf{y})$ is $\mathcal{O}(n^3 \log n)$ which is comparable with $\mathcal{O}(n^3)$ operation count associated with the straightforward computation of $R_{FBP}^{-1}R_{1/W}g(\mathbf{y})$. In the former case of small values of N computation of $R_{FBP}^{-1}R_{1/W}g(\mathbf{y})$ requires much less operations (of order of $\mathcal{O}(n^2 \log n)$); however, the total acceleration is not as dramatic since evaluation of $V(\mathbf{x},\varphi)$ still requires $\mathcal{O}(n^3)$ operations. (The acceleration effect can become more essential in the case when several reconstructions are required within the same section of the body, since in this case $V(\mathbf{x},\varphi)$ needs to be computed only once).

In general, replacement of the Fourier transforms by their discrete counterparts (FFTs) in equation (22) can lead to a spatial aliasing (wrap-around effect). In order to reduce this effect one would need to zero-pad the functions which, in turn, would result in an increase in computing time. In our numerical experiments, however, this effect turned out to be insignificant; all results presented in the next section were computed without zero-padding.

3.3 Numerical examples

In this section we present results of reconstructions from simulated projections computed using the inverse amplitude algorithm described above. We use this method to invert the attenuated Radon

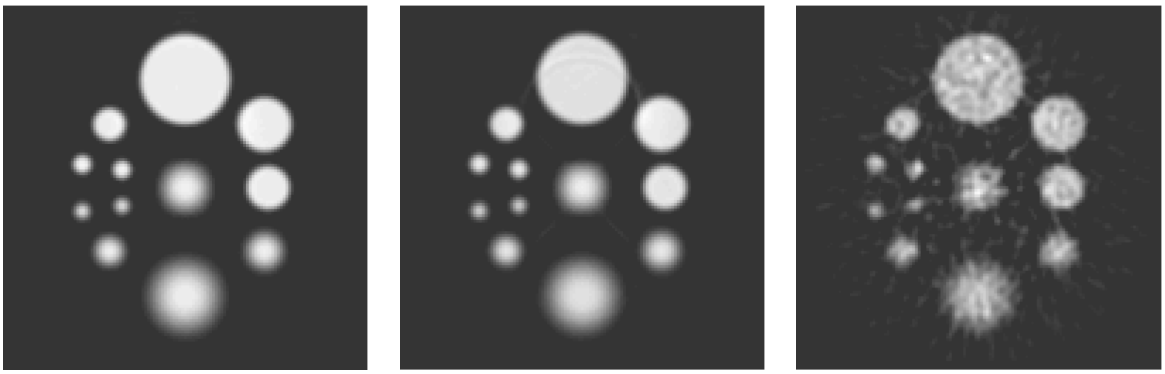

(a) (b) (c)

Figure 4: Images reconstructed using the inverse amplitude technique of Section 3 (a) case of smooth attenuation (see Figure 2(c)) (b) case of discontiuos attenuation (see Figure 2(b)) (c) discontinuous attenuation and noisy data; compare to Figure 3

transform with exponential weights, so that the results can be compared directly with the images obtained in Section 2.

As before, the model activity distribution presented in Figure 2(a) is utilized in all simulations within this section. We start with the case of smooth attenuation coefficient shown in Figure 2(c). Figure 4(a) demonstrates the image obtained using the basic version of our method given by equation (20) (without spectral domain computations). Although the method we use is not theoretically exact, the reconstruction is practically perfect in this case.

Our next simulation was done with the discontinuous attenuation phantom, Figure 2(b). Notice that the heuristic reasonings of the previous section were based on the results of the standard theory of ΨDO valid for smooth amplitudes. Nevertheless, as can be seen in Figure 4(b), our method produces quite accurate reconstructions even in the case of discontinuous attenuation. The only image imperfection noticeable in this figure is a slight circular line crossing the uppermost white circle.

Figure 4(c) presents an image reconstructed from noisy data in the presence of discontinuous attenuation. Exactly the same projection data were used as the one utilized in Section 2; the results of the reconstruction can be compared with images in Figures 3(b), 3(c), and 3(c). One can see that the inverse amplitude method is much less sensitive to noise and, in case of noisy data, it produces images of better quality than the ones obtained from techniques of Section 2.

Series of images presented in Figure 5 were obtained using the inverse amplitude method with computations carried out in the spectral domain, as explained in Section 3.2 . Figure 5(a) shows a result of reconstruction in the case of smooth attenuation (Figure 2(c)); only five terms ($N = 5$) of the series (22) were used in the computation; the image practically coincides with almost perfect image shown in Figure 4(a). Images shown in Figures 5(b), 5(c) correspond to reconstructions in the case of discontinuous attenuation, with $N = 5$ and $N = 30$ respectively. One can notice a little circular jump in brightness located across the uppermost white circle in the image in Figure 5(b). When larger number of harmonics is used (Figure 5(c)) the jump practically disappears; in this case the image is very close to the one shown in Figure 4(b) (inverse amplitude technique without spectral computations). Finally, image in Figure 5(d) was obtained from noisy projections corresponding to discontinuous attenuation coefficient; the low noise sensitivity of the algorithm is clearly seen (compare to Figures 4(c), 3(b), 3(c), and 3(d)). In general, comparing images of

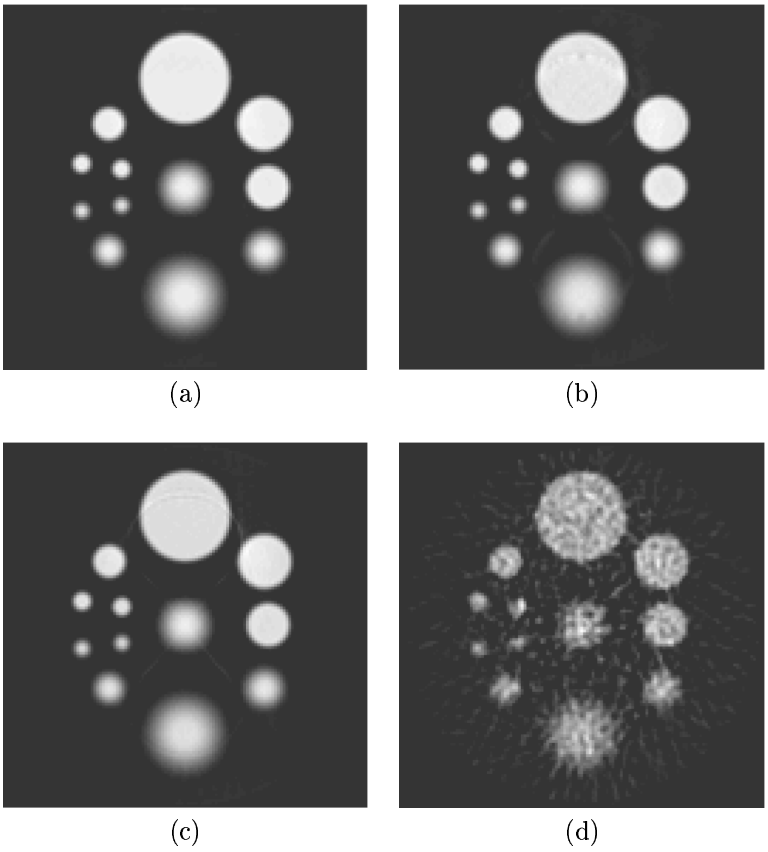

Figure 5: Images reconstructed using the inverse amplitude algorithm technique of Section 3 with computations in the spectral domain (Section 3.2 (a) case of smooth attenuation, $N = 5$ (b) case of discontiuos attenuation, $N = 5$ (c) case of discontiuos attenuation, $N = 30$ (d) case of discontinuous attenuation and noisy data, $N = 5$.

Figure 5 against those shown in Figure 4 one can notice that the inverse amplitude algorithm with computations in spectral domain yields slightly sharper images than the ones produced by this algorithm with straightforward computation of $R_{FBP}^{-1} R_{1/W} g(\mathbf{y})$. Explanation of this fact was provided in Section 3.2.

One can conclude from the numerical examples presented in this section that both versions of the inverse amplitude method we introduce are capable of reconstructing very close approximations from exact projections. On the other hand, these techniques are significantly less sensitive to noise than the method based on the explicit inversion formula (see Section 2). This low noise sensitivity enables one to process successfully results of real measurements as demonstrated in the next section.

4 Application to real data

In this Section we test the algorithms introduced in Sections 2 and 3 on data of real measurements. Images presented within this section were reconstructed from real measurements performed at the Service Hospitalier Frederic Joliot, France. The measurements were carried out using phantoms made of several cylindrical vessels filled with radiating and absorbing solutions. The corresponding

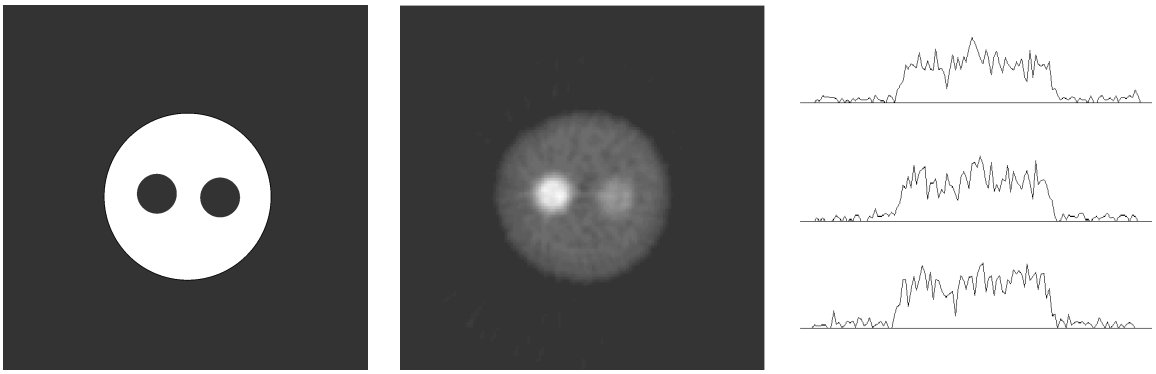

(a) (b) (c)

Figure 6: Real phantoms (a) activity distribution (b) attenuation map (c) some of the projections. Results of measurements courtesy Service Hospitalier Frederic Joliot, France.

activity distribution is shown in Figure 6(a). Figure 6(b) presents the attenuation distribution created in the experiment; the maximal optical length (a dimensionless quantity equal to a line integral from attenuation coefficient) was equal to 4.35. One can judge the level of noise in the actual projections from the graphs presented in Figure 6(c). (Notice that in the absence of noise the graphs corresponding to projections of the phantom shown in Figure 6(a) would be represented by a few almost circular arches; in our case, however, this structure is completely masked by the noise).

Images reconstructed using algorithms introduced in Sections2 and 3 are presented in Figure 7. Similarly to what was observed in numerical simulations of Section 2, the straightforward use of the explicit inversion formula yields an unacceptable level of noise in the image (Figure 7(b)), even if significant low-pass filtration (Figure 7(c)) is applied. The multiplicative correction technique of Section 2.3 produces considerably less noisy image, see Figure 7(d). Both versions of the inverse amplitude algorithm (Section 3) yield even better reconstruction; in agreement with the discussion in the beginning of Section 3.2 the straightforward evaluation of $R^{-1}_{FBP} R_{1/W} g$ leads to a certain loss of finer details and produces slightly smoother image than the one reconstructed through evaluation of this operator in the spectral domain. (The latter method seems to be preferable since, if a smoother image is desired, one can always apply a low-pass filtration to a sharper image; on the other hand, producing a sharper image from a smoother one represents an ill-posed problem).

5 Conclusions and acknowledgments

In present paper we introduced two analytic methods applicable for image reconstruction in emission tomography. These algorithms were tested both by numerical simulations and by applying them to (noisy) data of real measurements.

The first of our methods is based on the Novikov explicit inversion formula; it can be used for the inversion of the attenuated Radon transform — this problem arises in SPECT. Our tests show that while the straightforward implementation of the formula works very well when no noise is present in the data, real measurements containing significant level of noise cannot be processed directly. As a remedy to this problem we introduced a multiplicative correction technique, which improves considerably the noise propagation properties of the algorithm. The combination of this

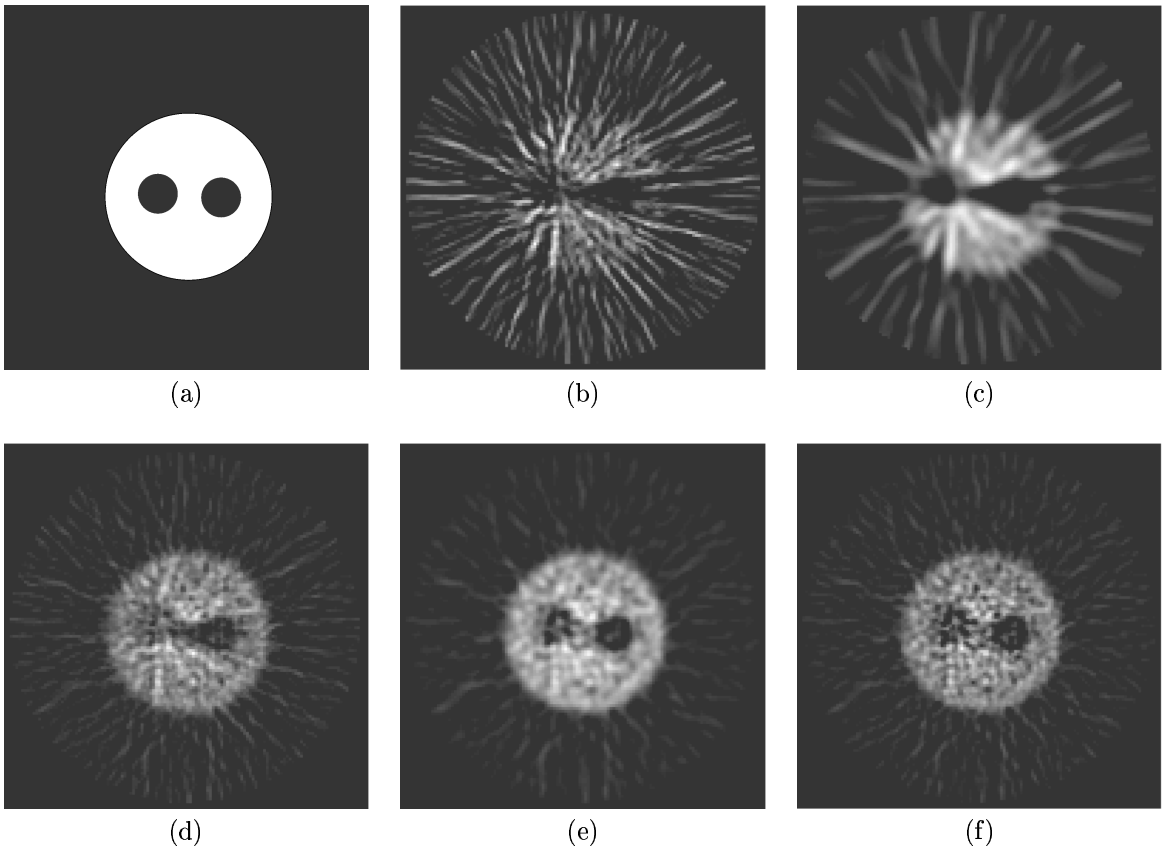

Figure 7: Reconstruction from real data (a) real activity distribution (b) Novikov inversion, see Section 3 (c) Novikov inversion with low-pass filtration (d) Novikov inversion with multiplicative correction, see Section refenhan (e) inverse amplitude algorithm of Section 3 (f) inverse amplitude algorithm with spectral computations (see Section 3.2). Results of measurements courtesy Service Hospitalier Frederic Joliot, France

technique with the explicit formula allows one to treat measurements containing high level of noise.

The second analytic method introduced in this paper can be used for approximate inversion of the (more general) weighted Radon transform, related to a wider variety of applications of emission tomography. Although this method is not exact, an extensive numerical testing demonstrates that it yields very accurate approximations in the case of exact data, and that this technique is very stable with respect to noise in the data — so that by processing real measurements with this algorithm one obtains better results than those resulting from theoretically exact computations. It is clear that the good performance of this technique is related to certain properties of ΨDO (as explained in Section 3), however, the rigorous theoretical foundation of the method is not available at this point; it is a subject of our current research.

We express our gratitude to Service Hospitalier Frederic Joliot, France, for the access to the data of real measurements. In particular, we would like to thank Dr. R. Trebossen for a detailed explanation of the structure of the phantom and measured data. We are also indebted to Professors R. Novikov, P. Kuchment and P. Guidotti for helpful discussions.

Appendix

In this Appendix we provide a derivation of equation (16). This formula results from equations (13), (14), and (15) after the following (self-explanatory) equivalent transformations:

$$
\begin{aligned}
g(\mathbf{y}) &= \left(R^{-1}R_w f\right)(\mathbf{y}) \\
&= \frac{1}{2}\int_0^{2\pi}\left\{\int_{\mathbb{R}}\left[\int_{\mathbb{R}}\left(\int_{\mathbb{R}^2} f(\mathbf{x})w(\mathbf{x},\omega(\varphi))\delta\left(\mathbf{x}\cdot\omega^{\perp}(\varphi)-p\right)\mathrm{d}\mathbf{x}\right)\mathrm{e}^{-2\pi\mathrm{i}p\rho}\mathrm{d}p\right]|\rho|\,\mathrm{e}^{2\pi\mathrm{i}\rho\mathbf{y}\cdot\omega^{\perp}(\varphi)}\mathrm{d}\rho\right\}\mathrm{d}\varphi \\
&= \frac{1}{2}\int_0^{2\pi}\int_0^{\infty}\int_{\mathbb{R}^2}|\rho|\,\mathrm{e}^{2\pi\mathrm{i}\rho(\mathbf{y}-\mathbf{x})\cdot\omega^{\perp}(\varphi)}f(\mathbf{x})w(\mathbf{x},\omega(\varphi))\mathrm{d}\mathbf{x}\;\mathrm{d}\rho\;\mathrm{d}\varphi \\
&\quad +\frac{1}{2}\int_0^{2\pi}\int_0^{\infty}\int_{\mathbb{R}^2}|\rho|\,\mathrm{e}^{2\pi\mathrm{i}\rho(\mathbf{y}-\mathbf{x})\cdot\omega^{\perp}(\varphi+\pi)}f(\mathbf{x})w(\mathbf{x},\omega(\varphi))\mathrm{d}\mathbf{x}\;\mathrm{d}\rho\;\mathrm{d}\varphi \\
&= \frac{1}{2}\int_{\mathbb{R}^2}\int_0^{2\pi}\int_0^{\infty}|\rho|\,\mathrm{e}^{2\pi\mathrm{i}\rho(\mathbf{y}-\mathbf{x})\cdot\omega^{\perp}(\varphi)}f(\mathbf{x})\left[w(\mathbf{x},\omega(\varphi))+w(\mathbf{x},\omega(\varphi+\pi))\right]\mathrm{d}\rho\mathrm{d}\varphi\mathrm{d}\mathbf{x} \\
&= \int_{\mathbb{R}^2}\int_{\mathbb{R}^2}\mathrm{e}^{2\pi\mathrm{i}(\mathbf{y}-\mathbf{x})\cdot\xi}f(\mathbf{x})W\left(\mathbf{x},\frac{\xi^{\perp}}{|\xi|}\right)\mathrm{d}\xi\mathrm{d}\mathbf{x},
\end{aligned}
$$

where the following notations were introduced

$$
\xi(\rho,\varphi) = \rho\omega^{\perp}(\varphi) = (\rho\cos\varphi,\rho\sin\varphi),
$$

$$
W(\mathbf{x},\omega) \equiv \frac{1}{2}\left[w(\mathbf{x},\omega)+w(\mathbf{x},-\omega)\right].
$$

References

[1] F. Natterer, *The mathematics of computerized tomography*, John Wiley & Sons, New York, 1986.

[2] N. G. Preobrazhensky and V. V. Pickalov, *Reconstructive Tomography in Gas Dynamics and Plasma Physics,* Nauka, Novosibirsk, 1987 (in Russian).

[3] H. Uchiyama, M. Nakajima, and S. Yuta, Measurement of Flame Temperature Distribution by IR Emission Computed Tomography, *Appl. Opt.*, **24**, p. 4111 (1985).

[4] H. M. Hertz and G. W. Faris, Emission tomography of flame radicals, *Optics Letters*, **13**, No 5, 351-353, (1988).

[5] L. A. Kunyansky, Automatization of noncontact diagnostics in technological processes of jet engine testing. Ph. D. Dissertation in Engineering, Kharkov Polytechnic Institute, Ukraine, 1992.

[6] C. L. Tien and S. C. Lee, Flame Radiation, *Progeress in Energy and Combustion Science*, **8**, No. 1, pp. 41-59 (1982).

[7] R. Novikov, An inversion formula for the attenuated X-ray transformation, *Ark. Mat.* (to be published).

[8] L. A. Kunyansky, A new SPECT reconstruction algorithm based on the Novikov explicit inversion formula, *Inverse Problems*, **17**, pp. 293-306 (2001).

[9] E. V. Arbuzov, A. L. Bukhgeim,. and S. G. Kazantsev, Two-dimensional tomography problems and the theory of A-analytic functions, *Siberian Advances in Mathematics*, **8**, no. 4, pp. 1-20 (1998).

[10] F. Natterer, Inversion of the attenuated Radon transform, *Inverse Problems*, **17**, pp 113-119 (2001).

[11] S. Bellini, M. Piacentini, C. Cafforio, and F. Rocca, Compensation of tissue absorption in emission tomography, *IEEE Trans. Acoust., Speech, Signal Processing,* ASSP-**27**, pp. 213-218 (1979).

[12] O. J. Tretiak and C. Metz., The exponential Radon transform, *Siam. J. Appl. Math.*, **39**, pp. 341-354 (1980).

[13] W. G. Hawkins, P. K. Leichner, and N. C. Yang, The circular harmonic transform for SPECT reconstruction and boundary conditions on the Fourier transform of the sinogram, *IEEE Trans. Med. Imag.,* **7**, pp. 135-148 (1988).

[14] T. Inouye, K. Kose, and A. Hasegawa, Image reconstruction algorithm for single-photon-emission computed tomography with uniform attenuation, *Phys. Med. Biol,* **34**, pp. 299-304 (1989).

[15] I. Ya. Shneberg, The exponential Radon transform. (Russian) *Dokl. Akad. Nauk SSSR,* **320** (1991), no. 3, pp. 567–571; translation in *Soviet Math. Dokl.* **44**, no. 2, pp. 512–516 (1992).

[16] I. Shneiberg, I. Ponomarev, V. Dmitrichenko, and S. Kalashnikov, On a new reconstruction algorithm in emission tomography, in *Applied Aspects of Radon Transform,* S.Gindikin (Ed.), AMS Transl, **162**, pp. 247-255 (1994).

[17] C. E. Metz and X. Pan, A unified analysis of exact methods of inverting the 2-D exponential Radon transform, with implications for noise control in SPECT, *IEEE Trans. Med. Imag.,* **14** , pp. 643-658 (1995).

[18] P. Kuchment and I. Shneiberg, Some inversion formulas in the Single Photon Emission Tomography, *Applicable Anal.*, **53**, pp. 221-231, (1994).

[19] P. Kuchment, On inversion and range characterization of one transform arising in emission tomography, *in Proceedings of the Conference "75 years of the Radon transform"*, Internat. Press, pp. 240-248 (1994).

[20] L. T. Chang, A method for attenuation correction in radionuclide computed tomography, *IEEE Trans. Nucl. Science,* **NS-25**, pp. 638-643 (1978).

[21] T. Morozumi, M. Nakajima, K. Ogawa and S. Yuta, Attenuation correction methods using the information of attenuation distribution for single photon emission CT, *Med. Imag. Tech.*, **2**, pp. 20-29 (1984).

[22] S. H. Manglos, R. I. Jaszczak, C. E. Floyd, L. J. Hahn, K. L. Greer, and R. E. Coleman, Nonisotropic attenuation in SPECT: Phantom tests of quantitative effects and compensation techniques, *J. Nucl. Med*, **28**, pp. 1584-1591 (1987).

[23] M. Singh, M. Horne, D. Maneval, J. Amartey J, and R. Brechner R, Non-uniform attenuation and scatter correction in SPECT *IEEE Trans. Nucl. Sci.* **35**, pt. 1, pp. 767-771, (1988).

[24] S. H. Manglos, R. I.. Jaszczak, and C. E. Floyd, Weighted backprojection implemented with a nonuniform attenuation map for improved quantitation *IEEE Trans. Nucl. Sci.* **35**, pt. 1, pp. 625-628 (1988).

[25] G. Bao and W. W. Symes, Computation of pseudo-differential operators *SIAM J. Sci. Comput.,* **17**, pp. 416-429 (1985).

[26] A. Markoe and E. T. Quinto, An elementary proof of local invertibility for generalized and attenuated Radon transforms, *Siam J. Math. Anal.*, **16**, pp. 1114-1119 (1985).

[27] J. Boman, Uniqueness theorems for generalized Radon transforms, *Preprint*, Department of Mathematics, Univ. of Stockholm, 1984.

[28] J. Boman, An example of non-uniqueness for a generalized Radon transform, *J. D'Analyse Mathematique,* **61**, 395-401 (1993).

[29] E. T. Quinto, The invertibility of rotation invariant Radon transforms, *J. Math. Anal. Appl.*, **91**, pp. 510-522 (1983).

[30] F. Treves, Intoruction to Pseudodifferential and Fourier Integral Operators, vol. 1, New York, Plenum Press, 1980.

[31] G. Beylkin, The inversion problem and applications of the generalized Radon transform, *Commun. Pure Appl. Math.*, **37**, No 5, pp. 579-599 (1984).

[32] L. A. Kunyansky, Generalized and attenuated Radon transforms: restorative approach to the numerical inversion, *Inverse Problems,* **8**, pp. 809-819 (1992).